

Agroseismology and the impact of farming practices on soil hydrodynamics

by Shi, Q., Montgomery, D.R., Swann, A.L.S., Cristea, N.C., Williams, E.F., You, N., Jeffrey, S., Collins, J., Barrio, A.P., Misiewicz, P.A., Nissen-Meyer, T. and Denolle, M.A.

Copyright, publisher and additional Information: This is the author accepted manuscript. The final published version (version of record) is available online via American Association for the Advancement of Science.

Please refer to any applicable terms of use of the publisher.

[DOI link to the version of record on the publisher's website](#)



**Harper Adams
University**

Shi, Q., Montgomery, D.R., Swann, A.L.S., Cristea, N.C., Williams, E.F., You, N., Jeffrey, S., Collins, J., Barrio, A.P., Misiewicz, P.A., Nissen-Meyer, T. and Denolle, M.A. (2026) 'Agroseismology and the impact of farming practices on soil hydrodynamics', *Science*, 392(6795), article number aec0970, pp. 306-310.

37 **Main Text:**

38 Soils form our planet's thin yet vital skin—a dynamic interface where the atmosphere meets solid
39 Earth, governing the exchange of water, carbon, and energy while underpinning agricultural
40 productivity, climate regulation, and landscape stability. At the heart of these functions lies the
41 porous architecture of soil, which controls water retention and movement, thereby shaping surface
42 and subsurface hydrological responses (1). Natural structures that develop over decades through
43 intertwined biological and geomorphological processes can be disrupted by land management with
44 far-reaching consequences for subsurface water dynamics central to soil ecosystems (2),
45 evapotranspiration and energy fluxes essential for land surface modeling and climate dynamics (3),
46 mechanical properties relevant to geotechnical and earthquake engineering (4), and moisture
47 availability and resilience in agriculture (5). Nevertheless, most land surface and hydrological
48 models treat soil as a static medium, overlooking its time-varying properties (6) and the effects of
49 repeated mechanical disturbance.

50 Current approaches of measuring soil hydrological response and properties include both ground-
51 based methods using point measurements with *in-situ* sensors (e.g., pressure transducers,
52 tensiometers, time-domain reflectometry, capacitance, impedance sensors, thermal probes (6)) and
53 non-invasive sensing (e.g., cosmic-ray neutron sensing, global navigation satellite systems
54 reflectometry, gamma-ray monitoring, ground-penetrating radar (7)). However, spatial
55 heterogeneity complicates the scaling of ground-based measurements across large areas. Satellite
56 and airborne sensing provide coarse (tens of kilometers) regional and global coverage (8), while
57 higher-resolution products from synthetic aperture radar carry sub-kilometer spatial resolution (9,
58 10) but suffer from low temporal resolution (days to months) and are sensitive to vegetation,
59 surface roughness, and atmospheric noise, limiting their ability to resolve fine-scale and short-term
60 soil moisture dynamics. Each approach trades spatial coverage for temporal resolution.

61 As structural changes in soils significantly influence stiffness and seismic wave speeds (11),
62 seismological methods have recently emerged as a powerful tool for continuous, spatially
63 distributed monitoring of subsurface hydromechanical properties from changes in seismic
64 velocities (dv/v) that have been shown to vary with groundwater and soil moisture levels (12–
65 16). Modeled as responses to pore pressure changes driven by rainfall diffusion (12, 14) under the
66 assumption of nonlinear elasticity in saturated media (17, 18), such correlations have enabled
67 empirical assessments of droughts (13, 16, 19, 20). Yet, to date, the approach remains site-specific
68 and requires local tuning to explain observations (e.g., (18)).

69 Distributed acoustic sensing (DAS) transforms standard fiber-optic cables into dense seismic
70 arrays with meter-scale spatial resolution, sub-minute temporal resolution, and broad frequency
71 sensitivity, allowing detection of shear-wave velocity changes linked to near-surface moisture
72 variability and soil stiffness (21). The utilization of fiber-optic cables enables continuous
73 monitoring of soil hydrodynamics over kilometers at meter-scale resolution, addressing the scale
74 gap between traditional point sensors and remote sensing. Here, we leveraged DAS and
75 hydromechanical modeling to characterize the seismic signature of soil in an experimental farm

76 where long-term tillage and compaction treatments have consistently altered soil structure. This
77 experimental farm provides a rare opportunity to test how controlled disturbance regimes impact
78 soil hydromechanics. By integrating DAS with physically grounded models, we unravel how
79 dynamic soil properties mediate the coupling between water fluxes and mechanical stability, with
80 fundamental implications for agriculture, land surface modeling, and geotechnical risk analysis.

81

82 **Turning fiber-optic cables into soil-health sensor networks**

83 From March 17 to 19, 2023, we conducted a DAS experiment at Harper Adams University, UK
84 (52.782°N, 2.428°W) across 27 ~4-meter-wide plots, each receiving consistent combinations of
85 tillage and compaction since 2011 (Fig. 1). Tillage had been applied at three depths commonly
86 used in farming—no tillage, 10 cm, and 25 cm—while compaction had been imposed using two
87 tire pressure levels—70 kPa for both front and rear tires, and 120 kPa for front and 150 kPa for
88 rear tires. Soil porosity measurements confirmed significant spatial variability across the plots (Fig.
89 1B). We deployed a fiber-optic cable perpendicular to plot boundaries in a finger-wide trench,
90 directly into the bare soil at ~2 cm depth to ensure good soil coupling (Fig. 1E). Using a Sintela
91 Onyx 1.0 DAS interrogator, we recorded 40 hours of continuous ambient seismic data at 2 kHz
92 sampling and 3.19 m channel spacing. Spectral analysis revealed one or two peaks: typically, a
93 fundamental mode around 15–25 Hz and an overtone near 25–50 Hz (fig. S1), consistent with
94 resonance from soft topsoil overlying stiff subsoil. These peak frequencies depend on topsoil
95 thickness and depth-integrated shear-wave velocity (v_s) (22). Episodes of broadband seismic
96 energy, including signals above 80 Hz, corresponded with rainfall and were consistent with
97 precipitation rate as the dominant control at these frequencies (23–25), with additional influences
98 from raindrop velocity (25) and droplet size (23). Simultaneously, we collected meteorological
99 data from a weather station ~500 m from the farm, including air temperature, humidity, and hourly
100 precipitation. Using the precipitation record, we calibrated DAS power spectral density in the 80–
101 140 Hz band as a 1-minute resolution proxy rain gauge (Fig. 1F and fig. S2). Additional variables
102 (cloud cover and wind speed) were obtained from another station ~700 m from the farm ((22) and
103 fig. S3). Overall, daily rainfall ranged from 5–10 mm, temperature from 5–15°C, humidity from
104 60–95% and wind speed (10-meter height) from 1–10 m/s.

105 We detected temporal changes in seismic velocity (dv/v), primarily reflecting changes in v_s (26),
106 using ambient noise auto-correlation functions (ACF; (27)) derived from DAS. ACFs were stable
107 over 15-second windows and showed coherent evolution between 15–60 Hz across plots (Fig. 1G,
108 figs. S4 and S5). A three-pass denoising and polynomial-fitting routine improved robustness,
109 especially during rapid dv/v fluctuations (e.g., after rainfall; fig. S6). The resulting dv/v time
110 series (e.g., Channel 18, hereafter as Ch 18; Fig. 1G) showed clear negative correlation with soil
111 water content: precipitation events (P1-P4) triggered sharp dv/v decreases, followed by gradual
112 recovery during drying. The dv/v response varied spatially, with some plots showing up to 60%
113 dv/v increase during drying (e.g., Ch 18; Fig. 1G), whereas others exhibited considerably lower

114 variability (e.g., Ch 33; fig. S5). We considered *precipitation, evapotranspiration, and drainage*
115 as the primary processes driving soil moisture dynamics (28).

116

117 **Physical models**

118 To interpret the observed seismic velocity changes, we built models that link soil water saturation
119 to shear-wave velocity by incorporating hysteretic, capillarity-controlled effective stress into
120 Hertz-Mindlin contact theory (29). Soil water saturation, S_w , is defined as the volumetric fraction
121 of water in pore space (11, 21). Our framework combined two elements: (i) a hydrological model
122 $H(\cdot)$ that captures how precipitation, evapotranspiration, and drainage control S_w , and (ii) a
123 lithological model $L(\cdot)$ that translates saturation changes into stiffness and seismic velocity.

124 The lithological model $L(\cdot)$ accounts for the impact of varying S_w on v_s . We started with $v_s =$
125 $\sqrt{\mu_{eff}/\rho}$, where both effective shear modulus μ_{eff} and density ρ depend on S_w . μ_{eff} derives
126 from Hertz-Mindlin theory (29), incorporating grain contact mechanics and S_w -dependent
127 effective pressure P_e (22). P_e includes a capillary suction, counteracted by gravity, enhancing soil
128 frame rigidity. Static suction stiffens soils during drying, but only dynamic capillarity—stresses
129 that depend on wetting or drying rates (30)—explains the observed short-term hysteresis in seismic
130 responses of some channels (fig. S7). Following (31), the dynamic capillary effect arises from
131 finite water redistribution times in the pore networks and is thus dependent on hydraulic
132 conductivity and meteorological forcing.

133 The hydrological model $H(\cdot)$ tracks the balance between precipitation, drainage, and
134 evapotranspiration, following (28): $S_w(t) = P(t) - Q(t) - ET(t)$, where P is precipitation, Q is
135 vertical drainage, and ET is evapotranspiration. We parameterized the drainage with an
136 exponential decay (~ 70 -hour timescale) of the precipitation input, similar to a baseflow model (32),
137 and estimated ET from weather data (Fig. 1F) using the Penman-Monteith equation (33), adjusted
138 for treatment effects (22).

139 We tested the combined model $v_s = L[H(P, Q, ET)]$ against observed velocities $v^{obs} = v_{s,ref} * (1 + dv/v)$
140 taking $v_{s,ref}$ immediately after the P4 rainfall event. Clay- and sand-type soil textures
141 represent endmember grain contacts: with more cohesive grain-to-grain contacts, clay defines the
142 upper bound of stiffness, while sand defines the lower bound. In addition, we tested capillary
143 models (their absence, or whether they are static or dynamic) across channels. The parameter space
144 for dynamic capillary coefficients is shown in Table S1. We illustrate two contrasting responses
145 to ET (March 18, 12:00; Fig. 2), which either exhibit strong temporal fluctuations at Ch 18 or do
146 not show any at Ch 33. The substantial v_s rise of 60% at Ch 18 was reproduced by dynamic
147 capillary pressure and a rapid decrease in S_w (as much as 50% in a single afternoon) driven by ET
148 (Fig. 2B), whereas static capillary effects explained only about half. In contrast, Ch 33 showed
149 low temporal variability (Fig. 2C) despite identical meteorological forcing. Other channels (e.g.,
150 Ch 44; fig. S8) showed intermediate variability, consistent with static capillary effects under high

151 hydrological variability. These stark differences, despite spatial proximity, indicate that structure
152 shaped by tillage and compaction is a dominant control, motivating a direct analysis of
153 hydrological variability across soil treatments.

154

155 **Connecting hydrodynamics with soil structure**

156 Based on our lithological model, moisture perturbations from a given hydrological process (e.g.,
157 drainage or evapotranspiration) are proportional to relative changes in v_s . This proportionality
158 reflects variability in pore-fluid pressure, with additional contributions from capillary effects (22);
159 Section 6: *Lithological Model* and fig. S9). The hydromechanical response is strongly modulated
160 by structural alterations from tillage and compaction. In the seismic analysis, we identified four
161 distinct styles of lithological responses that correspond to different combinations of tillage depth
162 and compaction pressure (Fig. 3A). All styles exhibit varying degrees of evaporation and drainage
163 shaped by specific near-surface regimes.

164 The primary contrast is between responses with negligible saturation changes over two days (Fig.
165 3A; green) and those exhibiting pronounced perturbations (Fig. 3A; red, orange, yellow). The
166 former corresponds to little or no tillage and reflects an unsaturated flow regime in which
167 precipitation or irrigation rapidly infiltrates into the vadose zone through well-connected pore and
168 micropore networks. The latter is associated with deep tillage, high compaction, or both, conditions
169 that disrupt pore connectivity, impede drainage, and promote transient near-surface saturation.
170 Common causes of such disruption include a compacted “plow-pan” layer at tillage depth, which
171 impedes vertical flow, and matrix collapse and macropore closure from mechanical disturbance
172 and high compaction (34). Evidence from the correlation between air humidity and soil saturation
173 beneath Ch 18 (Fig. 2A) indicates that moisture remained near the surface, without penetrating to
174 depth, and provides a clear demonstration of impaired hydraulic connectivity. These alterations
175 reduce permeability, limit infiltration depth, heighten sensitivity to surface evaporation, and
176 promote runoff and consequently erosion. In undisturbed soils, pore networks enable infiltration
177 to the root zone. In highly disturbed soils, reduced infiltration promotes near-surface saturation,
178 increasing runoff and evaporation, and thus delivering less moisture to the root zone (Fig. 4).

179 Three different styles of saturated response reflected treatment intensity. First, deep tillage and
180 high compaction both produced pronounced 5-hour evaporation and prolonged drainage, while the
181 combination of moderate tillage and compaction showed little evaporation (Fig. 3B), shorter
182 drainage durations, and slightly faster post-rain drainage (Fig. 3C). Insensitivity to evaporation
183 may result in persistently high saturation, suppressing capillary effects (Fig. 2C). Second,
184 evaporation rates also differed between extreme tillage and extreme compaction due to their
185 distinct impacts on pore structure. High surface loading pressure from traffic (Fig. 3A, dotted
186 contours) compacts near-surface soil, altering the vertical distribution of permeability and
187 aggregate connectivity. Hence, under shallow tillage and high compaction, micropores dominate
188 water flow, promoting prolonged “Stage I” evaporation supported by capillary rise and

189 maintaining hydraulic continuity to the surface. In contrast, deep tillage and low compaction may
190 disrupt near-surface pore networks and produce less efficient “Stage II” evaporation, which is
191 dominated by vapor diffusion from a receding drying front (35). In other words, seismic velocity
192 changes are governed by capillary contributions, particularly dynamic, rate-dependent effects,
193 which depend on how water is partitioned between micropores and macropores, features that are
194 highly sensitive to mechanical disturbance and thus motivate a quantitative measure of disturbance
195 across plots.

196 To quantify mechanical disturbance across plots, we parameterized tillage depth, T (cm), and
197 compaction expressed as tire pressure, C (kPa), into a disturbance index (DI). We chose a product
198 and power-law functional form $DI = T^n C^m$, normalized DI to between 0–1 and fit the cumulative
199 drainage $\delta(dv/v)$ for the exponents via grid search. We found the best-fitting values of $n = 0.22$
200 and $m = 0.96$ (fig. S10) and show the spatial variation of these correlations in Fig. 3D. Our results
201 confirm a strong impact of mechanical disturbance (Fig. 3A) on hydrological and hydromechanical
202 variability, consistent with previous reports (34). We modeled v_s across DAS channels based on
203 DI , which aligned with observed patterns in space and time (Fig. S11), demonstrating the
204 compounding effects of tillage and compaction on soil structure.

205 High- DI soils (Fig. 3A; red, orange, yellow) have decreased pore connectivity, heightened
206 capillary suction, and prolonged water redistribution. These dynamic capillary effects amplified
207 the soil’s response to atmospheric forcing, driving greater fluctuations in inter-particle stress and
208 in shallow moisture content during cycles of rainfall and evaporation. Over time, these effects can
209 contribute to pore-scale mechanical fatigue, likely weakening soil aggregates (36). Low- DI soils
210 (Fig. 3A; green) maintain well-connected pores, promoting deep infiltration and capillary
211 buffering, thereby stabilizing shallow moisture.

212 These hydraulic and hydromechanical effects are rooted in mechanical disturbances to the soil
213 structure. The sensitivity of seismic velocity to water saturation enables us to observe, in situ and
214 in real time, the coupling between pore connectivity, moisture retention, and hydrological
215 redistribution. By capturing both rapid hydrological fluxes and slow mechanical recovery, our
216 approach bridges the physical models proposed by hydrologists with the dynamic behavior
217 observed in the field, revealing how soil structures profoundly influence hydrological function.
218 These insights carry significant implications for guiding sustainable agriculture and water
219 management, as well as for improving models of land surface fluxes, carbon cycling, greenhouse
220 gas fluxes, and geotechnical risk across disturbed and undisturbed landscapes.

221

222 **Implications for agriculture and soil health**

223 This mechanistic insight is independent of sensing approaches, but its broader relevance depends
224 on resolving how mechanical disturbance shapes plant–soil interactions over full growing seasons
225 and across the root zone (~30–150 cm; (37)). Nonetheless, our results show that tillage-related
226 disturbance impairs moisture retention and thus drought resilience, an effect pertinent to

227 agricultural sustainability. Hence, adopting low-disturbance practices (e.g., no- or low-till farming)
228 can serve as a potential climate adaptation to preserve the soil's structural capacity to buffer against
229 drought and seasonal water stress. Continuous DAS monitoring can provide seasonal and longer
230 measures of hydrologic flux, though evolving surface conditions, variable coupling, and
231 interruptions from farming operations remain practical challenges. DAS enables battery-free,
232 permanent sensing with kilometer-scale reach from a single interrogator. In agricultural settings,
233 fibers can be installed alongside and between planting rows, enabling minimally intrusive,
234 repeated monitoring of hydromechanical processes and facilitating the implementation of
235 precision irrigation. Advances in DAS edge computing now allow on-site extraction of low-
236 volume, process-level data products without retaining raw waveforms (38), supporting real-time
237 integration with in-situ moisture probes and remote sensing. Benchmarked across multiple
238 channels, this framework provides a scalable model that can be calibrated across diverse settings
239 and establishes a quantitative baseline for future integration with direct soil moisture observations.
240 Once validated across soil types and farming systems, such hybrid deployments could offer a low-
241 labor, dense, and durable means of observing the subsurface moisture dynamics that govern
242 agricultural resilience.

243

244 **Implications for Earth system modelling**

245 Beyond the farm scale, soil–water interactions carry implications for how land–atmosphere
246 exchanges are represented in climate models. Although soil structure and pore connectivity exert
247 first-order controls on these exchanges (39), the evolution of soil pore structure is largely omitted
248 by current hydrologic and land-surface models (40), even though the omission is recognized as a
249 major unresolved problem in hydrology and groundwater recharge (41). Our results outline a
250 pathway to address this gap by tracking soil structure through time and with land-management
251 changes, and by incorporating rate-dependent capillarity to refine estimates of *ET*, runoff, and
252 groundwater recharge (e.g., Fig S12). This would add process-level constraints to complement
253 traditional energy-based *ET* schemes. While model tuning in our framework parallels existing
254 land-surface calibration (42), our approach anchors estimates to pore-scale hydromechanical
255 behavior.

256 At kilometer scales, Earth system models rely on aggregated soil–atmosphere flux
257 parameterizations (43) and sub-grid tiling (40). Because soil structure governs moisture
258 availability and energy exchange, these parameterizations require finer constraints. DAS helps
259 bridge this gap by delivering meter-scale, continuous measurements over tens of kilometers,
260 enabling translation of plot-scale hydromechanical processes into landscape- and watershed-scale
261 flux estimates. Our results show that fiber-optic sensing can sharpen land-surface flux
262 parameterizations and support more robust climate-relevant land-surface modeling.

263

264 **Implications for geotechnical engineering**

265 Moisture-dependent stiffness also impacts seismic hazard and infrastructure stability. Although
266 near-surface v_s is a standard input to seismic site response models (44), our results show that
267 moisture-driven, capillary-induced changes challenge the assumption of a static geotechnical layer.
268 This aligns with growing evidence that groundwater fluctuations and seasonal variability can
269 modify site response and promote ground failure (45, 46). Earthquake-triggered liquefaction,
270 traditionally considered limited to fully saturated soil, may also occur in partially saturated soil
271 (47) once a percolation threshold is exceeded (~70% saturation), and water levels remain a key
272 control on failure potential (48). As climate variability and urbanization alter near-surface
273 hydrology, incorporating the effects of hydrological processes on soil stability becomes essential
274 for assessing ground failure and designing resilient infrastructure. Our fiber-optic sensing
275 approach could enable in-situ monitoring of geostuctures and real-time feedback on evolving
276 stiffness as part of long-term infrastructure surveillance.

277

278

279 References and Notes

- 280 1. H.-J. Vogel, M. Balseiro-Romero, A. Kravchenko, W. Otten, V. Pot, S. Schlüter, U. Weller,
281 P. C. Baveye, A holistic perspective on soil architecture is needed as a key to soil functions.
282 *Eur. J. Soil Sci.* **73**, e13152 (2022).
- 283 2. H. Vereecken, A. Schnepf, J. W. Hopmans, M. Javaux, D. Or, T. Roose, J. Vanderborght,
284 M. H. Young, W. Amelung, M. Aitkenhead, S. D. Allison, S. Assouline, P. Baveye, M.
285 Berli, N. Brüggemann, P. Finke, M. Flury, T. Gaiser, G. Govers, T. Ghezzehei, P. Hallett,
286 H. J. Hendricks Franssen, J. Heppell, R. Horn, J. A. Huisman, D. Jacques, F. Jonard, S.
287 Kollet, F. Lafolie, K. Lamorski, D. Leitner, A. McBratney, B. Minasny, C. Montzka, W.
288 Nowak, Y. Pachepsky, J. Padian, N. Romano, K. Roth, Y. Rothfuss, E. C. Rowe, A.
289 Schwen, J. Šimůnek, A. Tiktak, J. Van Dam, S. E. A. T. M. van der Zee, H. J. Vogel, J. A.
290 Vrugt, T. Wöhling, I. M. Young, Modeling soil processes: Review, key challenges, and
291 new perspectives. *Vadose Zone J.* **15**, vzj2015.09.0131 (2016).
- 292 3. M. Stéfanon, P. Drobinski, F. D'andrea, C. Lebeau-pin-brossier, S. Bastin, Soil moisture-
293 temperature feedbacks at meso-scale during summer heat waves over Western Europe.
294 *Clim. Dyn.* **42**, 1309–1324 (2014).
- 295 4. M. G. Gomez, B. C. Martinez, J. T. DeJong, C. E. Hunt, L. A. deVlaming, D. W. Major, S.
296 M. Dworatzek, Field-scale bio-cementation tests to improve sands. *Proc. Inst. Civ. Eng. -*
297 *Ground Improv.* **168**, 206–216 (2015).
- 298 5. D. R. Montgomery, Soil security and global food security. *Front. Agric. Sci. Eng.* **11**, 297–
299 302 (2024).
- 300 6. H. Vereecken, W. Amelung, S. L. Bauke, H. Bogen, N. Brüggemann, C. Montzka, J.
301 Vanderborght, M. Bechtold, G. Blöschl, A. Carminati, M. Javaux, A. G. Konings, J.
302 Kusche, I. Neuweiler, D. Or, S. Steele-Dunne, A. Verhoef, M. Young, Y. Zhang, Soil
303 hydrology in the Earth system. *Nat. Rev. Earth Environ.* **3**, 573–587 (2022).

- 304 7. H. R. Bogen, J. A. Huisman, A. Güntner, C. Hübner, J. Kusche, F. Jonard, S. Vey, H.
305 Vereecken, Emerging methods for noninvasive sensing of soil moisture dynamics from
306 field to catchment scale: a review. *WIREs Water* **2**, 635–647 (2015).
- 307 8. E. Babaeian, M. Sadeghi, S. B. Jones, C. Montzka, H. Vereecken, M. Tuller, Ground,
308 proximal, and satellite remote sensing of soil moisture. *Rev. Geophys.* **57**, 530–616 (2019).
- 309 9. B. Bauer-Marschallinger, V. Freeman, S. Cao, C. Paulik, S. Schaufler, T. Stachl, S.
310 Modanesi, C. Massari, L. Ciabatta, L. Brocca, W. Wagner, Toward global soil moisture
311 monitoring with Sentinel-1: Harnessing assets and overcoming obstacles. *IEEE Trans.*
312 *Geosci. Remote Sens.* **57**, 520–539 (2019).
- 313 10. Y. Izumi, Widodo ,J., Kausarian ,H., Demirci ,S., Takahashi ,A., Razi ,P., Nasucha ,M.,
314 Yang ,H., J. and Tetuko S. S., Potential of soil moisture retrieval for tropical peatlands in
315 Indonesia using ALOS-2 L-band full-polarimetric SAR data. *Int. J. Remote Sens.* **40**, 5938–
316 5956 (2019).
- 317 11. S. G. Solazzi, L. Bodet, K. Holliger, D. Jougnot, Surface-wave dispersion in partially
318 saturated soils: The role of capillary forces. *J. Geophys. Res. Solid Earth* **126**,
319 e2021JB022074 (2021).
- 320 12. Q.-Y. Wang, F. Brenguier, M. Campillo, A. Lecointre, T. Takeda, Y. Aoki, Seasonal crustal
321 seismic velocity changes throughout Japan. *J. Geophys. Res. Solid Earth* **122**, 7987–8002
322 (2017).
- 323 13. T. Clements, M. A. Denolle, Tracking groundwater levels using the ambient seismic field.
324 *Geophys. Res. Lett.* **45**, 6459–6465 (2018).
- 325 14. C. Donaldson, T. Winder, C. Caudron, R. S. White, Crustal seismic velocity responds to a
326 magmatic intrusion and seasonal loading in Iceland’s Northern Volcanic Zone. *Sci. Adv.* **5**,
327 eaax6642 (2019).
- 328 15. L. Illien, C. Andermann, C. Sens-Schönfelder, K. L. Cook, K. P. Baidya, L. B. Adhikari, N.
329 Hovius, Subsurface moisture regulates Himalayan groundwater storage and discharge. *AGU*
330 *Adv.* **2**, e2021AV000398 (2021).
- 331 16. S. Mao, W. L. Ellsworth, Y. Zheng, G. C. Beroza, Depth-dependent seismic sensing of
332 groundwater recovery from the atmospheric-river storms of 2023. *Science* **387**, 758–763
333 (2025).
- 334 17. P. A. Johnson, P. N. J. Rasolofosaon, Nonlinear elasticity and stress-induced anisotropy in
335 rock. *J. Geophys. Res. Solid Earth* **101**, 3113–3124 (1996).
- 336 18. T. Clements, M. A. Denolle, The seismic signature of California’s earthquakes, droughts,
337 and floods. *J. Geophys. Res. Solid Earth* **128**, e2022JB025553 (2023).
- 338 19. S. Zhang, B. Luo, Y. Ben-Zion, D. E. Lumley, H. Zhu, Monitoring terrestrial water storage,
339 drought and seasonal changes in central Oklahoma with ambient seismic noise. *Geophys.*
340 *Res. Lett.* **50**, e2023GL103419 (2023).

- 341 20. K.-F. Feng, M. Denolle, F.-C. Lin, T. van Dam, A decadal survey of the near-surface
342 seismic velocity response to hydrological variations in Utah, United States. *Journal of*
343 *Geophysical Research Solid Earth* **131**, e2024BO30689 (2024).
- 344 21. Z. Shen, Y. Yang, X. Fu, K. H. Adams, E. Biondi, Z. Zhan, Fiber-optic seismic sensing of
345 vadose zone soil moisture dynamics. *Nat. Commun.* **15**, 6432 (2024).
- 346 22. Materials and methods are available as supplementary materials.
- 347 23. N. I. Fox, The representation of rainfall drop-size distribution and kinetic energy. *Hydrol.*
348 *Earth Syst. Sci.* **8**, 1001–1007 (2004).
- 349 24. T. Dean, The seismic signature of rain. *GEOPHYSICS* **82**, P53–P60 (2017).
- 350 25. E. J. Rindraharisaona, A. Réchou, F. R. Fontaine, G. Barruol, P. Stamenoff, B.
351 Boudevillain, F. Rigaud-Louise, E. Delcher, Seismic signature of rain and wind inferred
352 from seismic data. *Earth Space Sci.* **9**, e2022EA002328 (2022).
- 353 26. R. Hennino, N. Trégourès, N. M. Shapiro, L. Margerin, M. Campillo, B. A. van Tiggelen,
354 R. L. Weaver, Observation of equipartition of seismic waves. *Phys. Rev. Lett.* **86**, 3447–
355 3450 (2001).
- 356 27. R. Snieder, A. Grêt, H. Douma, J. Scales, Coda wave interferometry for estimating
357 nonlinear behavior in seismic velocity. *Science* **295**, 2253–2255 (2002).
- 358 28. M. O. Stahl, K. A. McColl, The seasonal cycle of surface soil moisture. *Journal of Climate*
359 **35**, 4997–5012. doi: 10.1175/JCLI-D-21-0780.1 (2022).
- 360 29. R. D. Mindlin, Compliance of elastic bodies in contact. *J. Appl. Mech.* **16**, 259–268 (1949).
- 361 30. T. Sakaki, D. M. O’Carroll, T. H. Illangasekare, Direct quantification of dynamic effects in
362 capillary pressure for drainage–wetting cycles. *Vadose Zone J.* **9**, 424–437 (2010).
- 363 31. R. Juanes, Nonequilibrium effects in models of three-phase flow in porous media. *Adv.*
364 *Water Resour.* **31**, 661–673 (2008).
- 365 32. C. Sens-Schönfelder, U. Wegler, Passive image interferometry and seasonal variations of
366 seismic velocities at Merapi Volcano, Indonesia. *Geophys. Res. Lett.* **33** (2006).
- 367 33. R. G. Allen, Food and Agriculture Organization of the United Nations, Eds., *Crop*
368 *Evapotranspiration: Guidelines for Computing Crop Water Requirements* (Food and
369 Agriculture Organization of the United Nations, Rome, 1998) *FAO irrigation and drainage*
370 *paper*.
- 371 34. M. W. Strudley, T. R. Green, J. C. Ascough, Tillage effects on soil hydraulic properties in
372 space and time: State of the science. *Soil Tillage Res.* **99**, 4–48 (2008).

- 373 35. A. Romero-Ruiz, N. Linde, L. Baron, D. Breitenstein, T. Keller, D. Or, Lasting effects of
374 soil compaction on soil water regime confirmed by geoelectrical monitoring. *Water Resour.*
375 *Res.* **58**, e2021WR030696 (2022).
- 376 36. D. R. Montgomery, Soil erosion and agricultural sustainability. *Proc. Natl. Acad. Sci.* **104**,
377 13268–13272 (2007).
- 378 37. J. Fan, B. McConkey, H. Wang, H. Janzen, Root distribution by depth for temperate
379 agricultural crops. *Field Crops Res.* **189**, 68–74 (2016).
- 380 38. Y. Ni, M. A. Denolle, Q. Shi, B. P. Lipovsky, S. Pan, J. N. Kutz, Wavefield reconstruction
381 of distributed acoustic sensing: Lossy compression, wavefield separation, and edge
382 computing. *J. Geophys. Res. Mach. Learn. Comput.* **1**, e2024JH000247 (2024).
- 383 39. C. M. Zarakas, D. Kennedy, K. Dagon, D. M. Lawrence, A. Liu, G. Bonan, C. Koven, D.
384 Lombardozi, A. L. S. Swann, Land processes can substantially impact the mean climate
385 State. *Geophys. Res. Lett.* **51**, e2024GL108372 (2024).
- 386 40. M. P. Clark, Y. Fan, D. M. Lawrence, J. C. Adam, D. Bolster, D. J. Gochis, R. P. Hooper,
387 M. Kumar, L. R. Leung, D. S. Mackay, R. M. Maxwell, C. Shen, S. C. Swenson, X. Zeng,
388 Improving the representation of hydrologic processes in Earth System Models. *Water*
389 *Resour. Res.* **51**, 5929–5956 (2015).
- 390 41. G. Blöschl, M. F. P. Bierkens, A. Chambel, C. Cudenneq, G. Destouni, A. Fiori, J. W.
391 Kirchner, J. J. McDonnell, H. H. G. Savenije, M. Sivapalan, C. Stump, E. Toth, E. Volpi,
392 G. Carr, C. Lupton, J. Salinas, B. Széles, A. Viglione, H. Aksoy, S. T. Allen, A. Amin, V.
393 Andréassian, B. Arheimer, S. K. Aryal, V. Baker, E. Bardsley, M. H. Barendrecht, A.
394 Bartosova, O. Batelaan, W. R. Berghuijs, K. Beven, T. Blume, T. Bogaard, P. Borges de
395 Amorim, M. E. Böttcher, G. Boulet, K. Breinl, M. Brilly, L. Brocca, W. Buytaert, A.
396 Castellarin, A. Castelletti, X. Chen, Y. Chen, Y. Chen, P. Chiffard, P. Claps, M. P. Clark,
397 A. L. Collins, B. Croke, A. Dathe, P. C. David, F. P. J. de Barros, G. de Rooij, G. Di
398 Baldassarre, J. M. Driscoll, D. Duethmann, R. Dwivedi, E. Eris, W. H. Farmer, J.
399 Feicabrino, G. Ferguson, E. Ferrari, S. Ferraris, B. Fersch, D. Finger, L. Foglia, K. Fowler,
400 B. Gartsman, S. Gascoïn, E. Gaume, A. Gelfan, J. Geris, S. Gharari, T. Gleeson, M.
401 Glendell, A. Gonzalez Bevacqua, M. P. González-Dugo, S. Grimaldi, A. B. Gupta, B. Guse,
402 D. Han, D. Hannah, A. Harpold, S. Haun, K. Heal, K. Helfricht, M. Herrnegger, M. Hipsey,
403 H. Hlaváčiková, C. Hohmann, L. Holko, C. Hopkinson, M. Hrachowitz, T. H.
404 Illangasekare, A. Inam, C. Innocente, E. Istanbuluoglu, B. Jarhani, Z. Kalantari, A.
405 Kalvans, S. Khanal, S. Khatami, J. Kiesel, M. Kirkby, W. Knoben, K. Kochanek, S.
406 Kohnová, A. Kolechkina, S. Krause, D. Kreamer, H. Kreibich, H. Kunstmann, H. Lange,
407 M. L. R. Liberato, E. Lindquist, T. Link, J. Liu, D. P. Loucks, C. Luce, G. Mahé, O.
408 Makarieva, J. Malard, S. Mashtayeva, S. Maskey, J. Mas-Pla, M. Mavrova-Guirguinova,
409 M. Mazzoleni, S. Mernild, B. D. Misstear, A. Montanari, H. Müller-Thomy, A. Nabizadeh,
410 F. Nardi, C. Neale, N. Nesterova, B. Nurtaev, V. O. Odongo, S. Panda, S. Pande, Z. Pang,
411 G. Papacharalampous, C. Perrin, L. Pfister, R. Pimentel, M. J. Polo, D. Post, C. Prieto
412 Sierra, M.-H. Ramos, M. Renner, J. E. Reynolds, E. Ridolfi, R. Rigon, M. Riva, D. E.
413 Robertson, R. Rosso, T. Roy, J. H. M. Sá, G. Salvadori, M. Sandells, B. Schaeffli, A.
414 Schumann, A. Scolobig, J. Seibert, E. Servat, M. Shafiei, A. Sharma, M. Sidibe, R. C.

- 415 Sidle, T. Skaugen, H. Smith, S. M. Spiessl, L. Stein, I. Steinsland, U. Strasser, B. Su, J.
416 Szolgay, D. Tarboton, F. Tauro, G. Thirel, F. Tian, R. Tong, K. Tussupova, H. Tyrallis, R.
417 Uijlenhoet, R. van Beek, R. J. van der Ent, M. van der Ploeg, A. F. Van Loon, I. van
418 Meerveld, R. van Nooijen, P. R. van Oel, J.-P. Vidal, J. von Freyberg, S. Vorogushyn, P.
419 Wachniew, A. J. Wade, P. Ward, I. K. Westerberg, C. White, E. F. Wood, R. Woods, Z.
420 Xu, K. K. Yilmaz, Y. Zhang, Twenty-three unsolved problems in hydrology (UPH) – a
421 community perspective. *Hydrol. Sci. J.* **64**, 1141–1158 (2019).
- 422 42. A. L. S. Swann, C. D. Koven, A Direct Estimate of the Seasonal Cycle of
423 Evapotranspiration over the Amazon Basin. doi: 10.1175/JHM-D-17-0004.1 (2017).
- 424 43. E. M. Blyth, V. K. Arora, D. B. Clark, S. J. Dadson, M. G. De Kauwe, D. M. Lawrence, J.
425 R. Melton, J. Pongratz, R. H. Turton, K. Yoshimura, H. Yuan, Advances in land surface
426 modelling. *Curr. Clim. Change Rep.* **7**, 45–71 (2021).
- 427 44. M. Geyin, B. W. Maurer, U.S. national VS30 models and maps informed by remote sensing
428 and machine learning. *Seismol. Res. Lett.* **94**, 1467–1477 (2023).
- 429 45. H. B. Okay, A. A. Özacar, A Novel VS30 Prediction strategy taking fluid saturation into
430 account and a new VS30 model of Türkiye. *Bull. Seismol. Soc. Am.* **114**, 1048–1065
431 (2023).
- 432 46. A. Händel, M. Pilz, L. C. Malatesta, D. Litwin, F. Cotton, Detecting seasonal differences in
433 high-frequency site response using κ_0 . *Seismica* **4** (2025).
- 434 47. A. Banerjee, A. J. Puppala, L. R. Hoyos, Liquefaction assessment in unsaturated soils. *J.*
435 *Geotech. Geoenvironmental Eng.* **148**, 04022067 (2022).
- 436 48. K. E. Allstadt, E. M. Thompson, R. W. Jibson, D. J. Wald, M. Hearne, E. J. Hunter, J. Fee,
437 H. Schovanec, D. Slosky, K. L. Haynie, The US Geological Survey ground failure product:
438 Near-real-time estimates of earthquake-triggered landslides and liquefaction. *Earthquake*
439 *Spectra* **38**, 5–36 (2022).
- 440 49. Q. Shi, M. Denolle, E. Williams, S. Jeffery, A. Barrio, P. Misiewicz, DAS observations in
441 Harper Adams University (2025); <https://doi.org/10.5061/dryad.0vt4b8hcb>.
- 442 50. Q. Shi, Agroseismology code (1.0). Zenodo (2025);
443 <https://doi.org/10.5281/zenodo.18040281>.
- 444 51. R. L. Weaver, O. I. Lobkis, Diffuse fields in open systems and the emergence of the
445 Green’s function (L). *J. Acoust. Soc. Am.* **116**, 2731–2734 (2004).
- 446 52. O. I. Lobkis, R. L. Weaver, “On the emergence of the Green’s function in the correlations
447 of a diffuse field” in *Seismic Interferometry: History and Present Status*, K. Wapenaar, D.
448 Draganov, J. O. A. Robertsson, M. A. Pelissier, Eds. (Society of Exploration Geophysicists,
449 2008; <https://doi.org/10.1190/1.9781560801924>)vol.. 26, p. 0.
- 450 53. C. Pacheco, R. Snieder, Time-lapse travel time change of multiply scattered acoustic waves.
451 *J. Acoust. Soc. Am.* **118**, 1300–1310 (2005).

- 452 54. T. Planès, Larose, Eric, Margerin, Ludovic, Rossetto, Vincent, C. and Sens-Schönfelder,
453 Decorrelation and phase-shift of coda waves induced by local changes: multiple scattering
454 approach and numerical validation. *Waves Random Complex Media* **24**, 99–125 (2014).
- 455 55. A. Colombi, J. Chaput, F. Brenguier, G. Hillers, P. Roux, M. Campillo, On the temporal
456 stability of the coda of ambient noise correlations. *Comptes Rendus Géoscience* **346**, 307–
457 316 (2014).
- 458 56. J. Li, W. Zhu, E. Biondi, Z. Zhan, Earthquake focal mechanisms with distributed acoustic
459 sensing. *Nat Commun* **14**, 4181 (2023).
- 460 57. M. B. Helgerud, J. Dvorkin, A. Nur, A. Sakai, T. Collett, Elastic-wave velocity in marine
461 sediments with gas hydrates: Effective medium modeling. *Geophys. Res. Lett.* **26**, 2021–
462 2024 (1999).
- 463 58. J. Dvorkin, M. Prasad, A. Sakai, D. Lavoie, Elasticity of marine sediments: Rock physics
464 modeling. *Geophys. Res. Lett.* **26**, 1781–1784 (1999).
- 465 59. X. García, E. A. Medina, Hysteresis effects studied by numerical simulations: Cyclic
466 loading-unloading of a realistic sand model. *Geophysics* **71**, F13–F20 (2006).
- 467 60. R. Bachrach, P. Avseth, Rock physics modeling of unconsolidated sands: Accounting for
468 nonuniform contacts and heterogeneous stress fields in the effective media approximation
469 with applications to hydrocarbon exploration. *Geophysics* **73**, E197–E209 (2008).
- 470 61. G. I. Barenblatt, Filtration of two nonmixing fluids in a homogeneous porous medium.
471 *Fluid Dyn.* **6**, 857–864 (1971).
- 472 62. S. M. Hassanizadeh, W. G. Gray, Mechanics and thermodynamics of multiphase flow in
473 porous media including interphase boundaries. *Adv. Water Resour.* **13**, 169–186 (1990).
- 474 63. F. J.-M. Kalaydjian, “Dynamic Capillary Pressure Curve for Water/Oil Displacement in
475 Porous Media: Theory vs. Experiment” (1992; <https://dx.doi.org/10.2118/24813-MS>).
- 476 64. S. M. Hassanizadeh, M. A. Celia, H. K. Dahle, Dynamic effect in the capillary pressure–
477 saturation relationship and its impacts on unsaturated flow. *Vadose Zone J.* **1**, 38–57
478 (2002).
- 479 65. H. K. Dahle, M. A. Celia, S. Majid Hassanizadeh, Bundle-of-tubes model for calculating
480 dynamic effects in the capillary-pressure-saturation relationship. *Transp. Porous Media* **58**,
481 5–22 (2005).
- 482 66. P. Talwani, L. Chen, K. Gahalaut, Seismogenic permeability, ks. *J. Geophys. Res. Solid*
483 *Earth* **112** (2007).
- 484 67. R. D. Andajani, T. Tsuji, R. Snieder, T. Ikeda, Spatial and temporal influence of rainfall on
485 crustal pore pressure based on seismic velocity monitoring. *Earth Planets Space* **72**, 177
486 (2020).

- 487 68. V. Sobolevskaia, J. Ajo-Franklin, F. Cheng, S. Dou, N. J. Lindsey, A. Wagner, Monitoring
488 water level of a surficial aquifer using distributed acoustic sensing and ballistic surface
489 waves. *Water Resour. Res.* **60**, e2023WR036172 (2024).
- 490 69. J. Kang, F. Walter, T. Halter, P. Paitz, A. Fichtner, Soil slope monitoring with Distributed
491 Acoustic Sensing under wetting and drying cycles. *Earth Surf. Dyn.* 13, 1133–1155 (2025).
- 492

493 **Acknowledgments:**

494 The authors sincerely thank Editor Angela Hessler and three anonymous reviewers for their
495 constructive comments and suggestions. The authors thank the University of Washington
496 FiberLab for instrumental support, and Dominik Gräff, Kuan-Fu Feng, and Jonathan Ajo-
497 Franklin for their helpful discussions.

498 **Funding:**

499 The Pan Family Fund (QS)
500 Murdock Charitable Trust (MD)
501 UW College of Env Seed Fund (AS)
502 Packard Foundation (MD)
503 NERC Cross-disciplinary research capability grant (TN)

504 **Author contributions:**

505 Conceptualization: MD, TN, SJ, QS, DM, NC
506 Methodology: QS, NY, MD
507 Investigation: QS, MD, NY, AS, EW, NC
508 Data curation: QS, EW, APB, JC, PM
509 Visualization: QS
510 Formal analysis: QS, MD
511 Validation: QS, MD, PM
512 Software: QS, NY
513 Funding acquisition: MD, TN, SJ, AS, DM, QS
514 Project administration: MD
515 Supervision: MD, DM, AS, NC, SJ
516 Writing – original draft: QS, MD
517 Writing – review & editing: QS, MD, DM, AS, NC, TN, SJ, PM, EW, NY, APB, JC

518 **Competing interests:** The Authors declare that they have no competing interests.

519

520 **Data and materials availability:**

521 The raw and processed data used in this study are available from Dryad (49). The software can
522 be accessed through Zenodo (50). The GitHub repository for this project is publicly accessible
523 at <https://github.com/Denolle-Lab/farmDAS/>. All other data needed to evaluate the
524 conclusions in the paper are present in the paper or the supplementary materials. No new
525 physical materials were generated for this study.

526

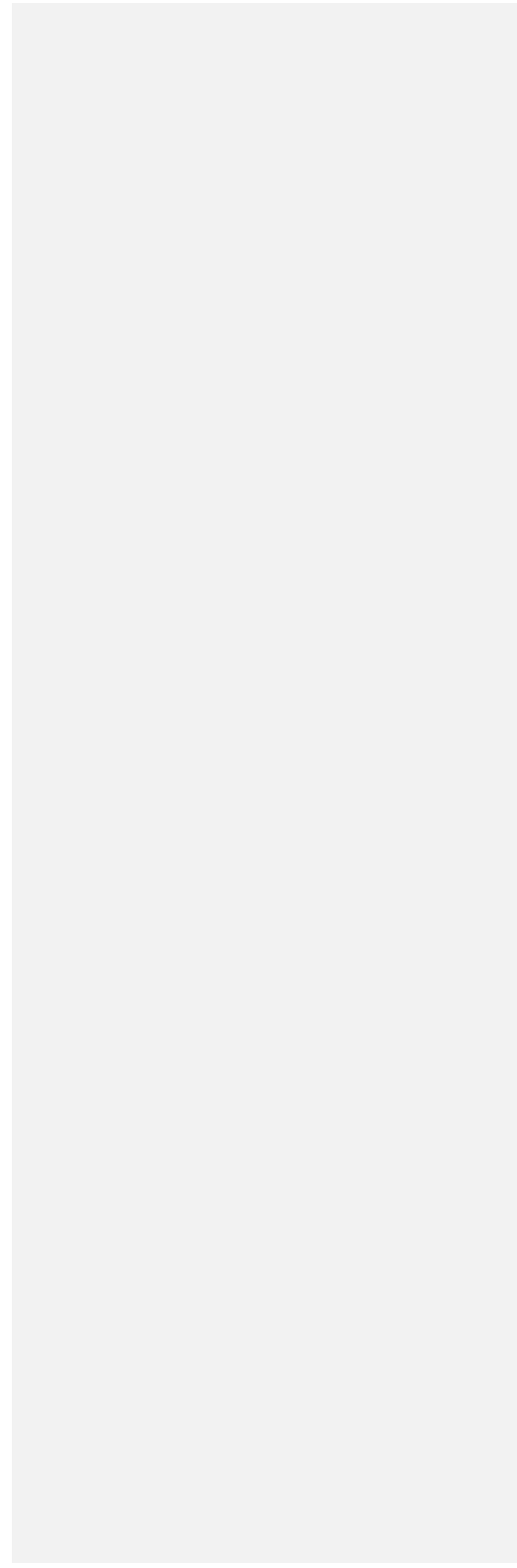
527 **Supplementary Materials**

Commented [AH1]: Neither of the links or DOIs in the reference list connected me to the correct repository. Please edit the reference list with an accurate DOI and url for (49) and (50).

Commented [QS2R1]: We have requested the dryad team to review our recent updates to the data. Once the dryad team finish the review, they will activate the link. We have corrected a typo in (49).

The zenodo link (50) should work.

528 Materials and Methods
529 Figs. S1 to S15
530 Table S1
531 Data S1
532 References (51–69)
533



534 **Fig. 1. Spatiotemporal variations of soil properties, treatments, and hydrological forcing.**

535 (A) Predicted shear-wave velocity (v_s) assuming saturated soil, shown at different depths and
536 locations along the cable. (B) Soil porosity at different depths and locations. (C) Degree of
537 compaction from tire pressure (C_{tire}) applied during traffic, interpolated onto DAS channels. (D)
538 Tilling depth (T_{till}) interpolated onto DAS channels. (E) Map of the research farm with the fiber-
539 optic cable indicated in light blue. (F) Precipitation rate highlighting four main rainfall events (P1-
540 P4), denoted by high-frequency DAS power spectral density, aligned with reference
541 evapotranspiration (ET_0) from net radiation and hourly weather conditions (symbols). (G)
542 Temporal changes in velocity over 40 hours at Channel 18 showing a sharp drop after rainfall,
543 together with the stretched auto-correlation functions (ACF).

544 **Fig. 2. Hydrological and lithological responses.**

545 (A) Water saturation (S_w) at Ch. 18 and Ch. 33 defined as the volumetric fraction of water in pore
546 space compared with air relative humidity. (B) Observed and modeled shear-wave velocity (v_s)
547 in response to lithological changes near the Ch. 18. (C) Same as (B), but for Ch. 33.

548 **Fig. 3. Spatial variability of mechanical disturbance.**

549 (A) Spatial variation of hydromechanical responses in relation to tillage depth and degree of
550 compaction measured by tire pressure. Four groups of dv/v curves (thin lines for individual
551 channels), each negatively correlated with water saturation, are located using their first data point
552 and color-coded in a traffic-light sequence according to relative hydrological response levels. The
553 average dv/v curves are shown in thick lines. Contour lines represent the disturbance index (DI)
554 and the relative impact of surface compaction on the tillage depth (stress ratio). (B) Velocity
555 changes governed by evapotranspiration (ET) during Period 1 in (A). (C) Velocity changes
556 governed by saturated versus unsaturated drainage during Period 2 in (A). (D) Disturbance Index
557 (dashed) and total velocity change (solid) along the cable during the drainage-dominated Period 2
558 in (A).

559 **Fig. 4. Conceptual model of effects of physical disturbance on soil hydrological response.**

560 (A) In undisturbed (untilled, uncompacted) soil, unsaturated drainage can retain more moisture at
561 the field capacity, enabling root water uptake. (B) In highly disturbed (tilled) soil, disrupted soil
562 structure leads to near-surface saturation, enhanced evaporation, and less moisture retained below
563 the tillage depth.